Supplementary Information: An Equivariant Graph Neural Network for the Elasticity Tensors of All Seven Crystal Systems

Mingjian Wen[1*], Matthew K. Horton[2,3], Jason M. Munro[2], Patrick Huck[4], Kristin A. Persson[5,6]

[1] Chemical and Biomolecular Engineering, University of Houston, Houston, 77204, TX, USA

[2] Materials Sciences Division, Lawrence Berkeley National Laboratory, Berkeley, 94720, CA, USA

[3] Microsoft Research, Redmond, 98052, WA, USA

[4] Energy Technologies Area, Lawrence Berkeley National Laboratory, Berkeley, 94720, CA, USA

[5] Molecular Foundry, Lawrence Berkeley National Laboratory, Berkeley, 94720, CA, USA

[6] Department of Materials Science and Engineering, University of California, Berkeley, Berkeley, 94720, CA, USA

The ten symmetry classes of elasticity tensors

Early approaches take inspiration from crystallography. Out of the 32 distinct crystallographic point groups, only 11 are centrosymmetric (meaning the point group contains an inversion center as one of its symmetry elements), each forming a unique diffraction pattern. The diffraction patterns of other noncentrosymmetric crystals each is the same as one of the 11 centrosymmetric crystals. Based on the diffraction patterns, the 32 distinct point groups can be categorized into 11 classes, called the Laue groups [3]. According to the Laue groups, Wallace [1] classifies the elasticity tensors into 12 classes (the additional 1 being the isotropic class that does not apply for single crystals), and they reduce to 10 classes considering the number of independent components (Fig. S1). The results are widely cited, including the classical book on the subject by Nye [2] and many recent papers [4–6]. This crystallographic approach seems reasonable; however, the conclusions are incorrect. The tetragonal and trigonal systems are each divided into two symmetry classes, but the distinctions can be eliminated by a different choice of the coordinate system [7, 8]. Then each of the tetragonal and trigonal systems will have 6 independent components.

Harmonic decomposition of the elasticity tensor

In the harmonic decomposition, the elasticity tensor can be written as

$$\boldsymbol{C} = h_1(\lambda) + h_2(\eta) + h_3(\boldsymbol{A}) + h_4(\boldsymbol{B}) + h_5(\boldsymbol{H}). \tag{1}$$

The appropriate values for each of the term is as follows:

$$\lambda = [2C_{ppmm} - C_{pmpm}]/15,$$

$$\eta = [-3C_{ppmm} - C_{pmpm}]/90,$$

*Email: mjwen@uh.edu

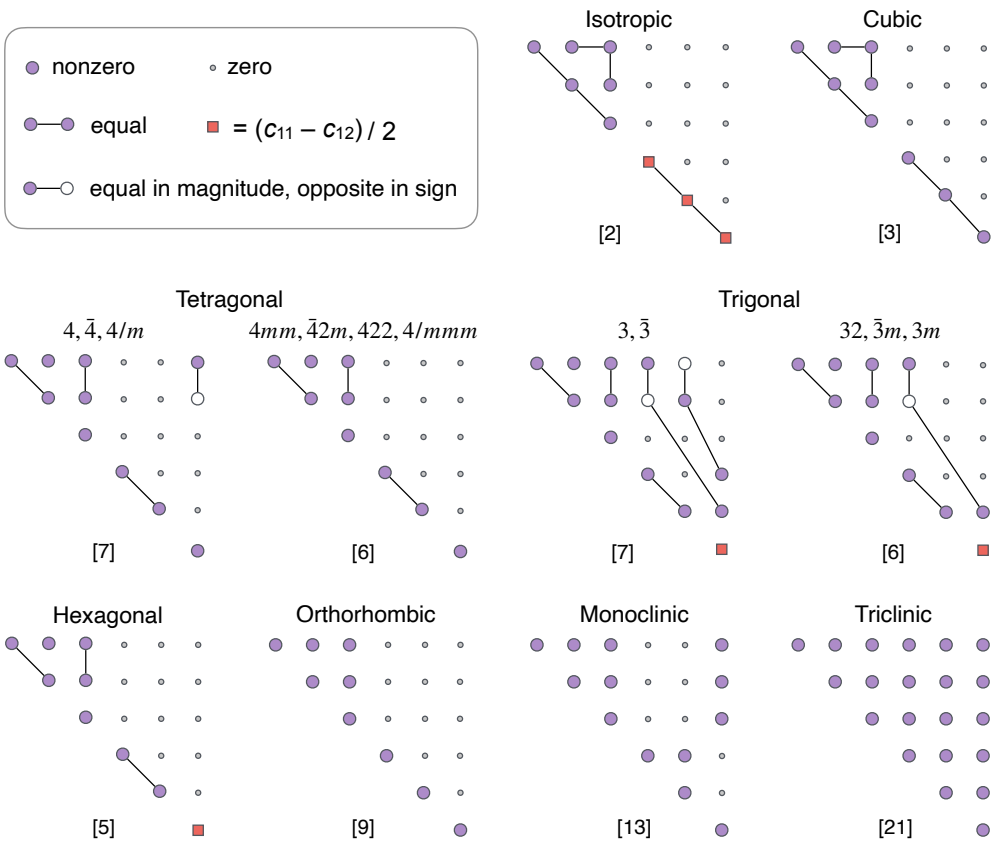

Figure S1: Symmetry classes and independent components of the stiffness tensor according to the crystallographic Laue group by Wallace [1]. There are 11 classes from Laue group, with two for the monoclinic system depending on the orientation. Here we only depict the one with the standard orientation. See Ref. 2 for the other case. The conclusion is incorrect for tetragonal and trigonal crystal systems—for each of them, there are two cases with 6 and 7 independent components. The value in the square brackets is the number of independent components for the corresponding crystal system. All matrices are symmetric about the leading diagonal, with the lower left part omitted in the depiction.

$$
\begin{aligned}
A_{ij} &= [15C_{ijmm} - 12C_{imjm} - 5\delta_{ij}C_{ppmm} + 4\delta_{ij}C_{pmpm}]/21, \\
B_{ij} &= [-6C_{ijmm} + 9C_{imjm} + 2\delta_{ij}C_{ppmm} - 3\delta_{ij}C_{pmpm}]/21, \\
H_{ijkl} =& (C_{ijkl} + C_{iklj} + C_{iljk})/3 \\
&- [(C_{ijmm} + 2C_{imjm})\delta_{kl} + (C_{klmm} + 2C_{kmlm})\delta_{ij} \\
&+ (C_{ikmm} + 2C_{imkm})\delta_{jl} + (C_{jlmm} + 2C_{jmlm})\delta_{ik} \\
&+ (C_{ilmm} + 2C_{imlm})\delta_{jk} + (C_{jkmm} + 2C_{jmkm})\delta_{il}]/21 \\
&+ (C_{ppmm} + 2C_{pmpm})(\delta_{ij}\delta_{kl} + \delta_{ik}\delta_{jl} + \delta_{il}\delta_{jk})/105,
\end{aligned}
$$

and

$$
\begin{aligned}
h_1(\lambda) &= \delta_{ij}\delta_{kl}\lambda, \\
h_2(\eta) &= (\delta_{ik}\delta_{jl} + \delta_{il}\delta_{jk})\eta, \\
h_3(\boldsymbol{A}) &= \delta_{ij}A_{kl} + \delta_{kl}A_{ij}, \\
h_4(\boldsymbol{B}) &= \delta_{ik}B_{jl} + \delta_{jl}B_{ik} + \delta_{il}B_{jk} + \delta_{jk}B_{il}, \\
h_5(\boldsymbol{H}) &= H_{ijkl},
\end{aligned}
$$

where δ_{ij} is the Kronecker delta.

This decomposition follows Ref. 9, and as mentioned there that "... other forms of harmonic decomposition are possible: It suffices to use invertible linear combinations of $\boldsymbol{A}$ and $\boldsymbol{B}$ and, analogously, invertible linear combinations of λ and η." See Ref. 10, 11 for such examples. Nevertheless, harmonic decomposition is unique to linear combinations.

This harmonic decomposition can be easily carried out with the `e3nn` package [12]. It can deal with any tensor of any symmetry, and below is a code snippet to obtain the irreducible representations of the elasticity tensor from the harmonic decomposition.

```
>>> from e3nn import o3, io

>>> tp = o3.ReducedTensorProducts("ijkl=jikl=ijlk=klij", i="1o")
>>> tp.irreps_out
2x0e+2x2e+1x4e

# Alternatively
>>> ct = io.CartesianTensor("ijkl=jikl=ijlk=klij")
>>> ct
2x0e+2x2e+1x4e
```

The `2x0e`, `2x2e`, and `4e` represent the two isotropic terms, the two deviatoric terms, and the harmonic term, respectively.

Proof of MatTen satisfying material symmetry

The MatTen model $\boldsymbol{C} = f(x)$ is equivariant to $SO(3)$ transformations, satisfying

$$D_y(g)f(x) = f(D_x(g)x). \tag{2}$$

This comes from the fact that each layer of MatTen is equivariant, and the composition of such layers is also equivariant. We refer to Ref. 13 for proof of the equivariance of the layers. The representation $D_x(g)$ in the space of crystal structures can be written as $D_x(g) = R_{ip}$, and the representation $D_y(g)$ in the space of stiffness tensors can be written as $D_g(g) = R_{ip}R_{jq}R_{kr}R_{ls}$, where $R \in SO(3)$ is a rotation matrix.

Let $Q \in P$, where P denotes the set of rotations in the point group of a crystal, we will have $P \subset SO(3)$. Therefore, for $R = Q$, Eq. S(2) is satisfied, i.e.,

$$Q_{ip}Q_{jq}Q_{kr}Q_{ls}C_{prqs} = f(Qx) \tag{3}$$

Owning to material symmetry, we have $Qx = x$, that is, the crystal structure x is indistinguishable before and after the transformation. Thus, $f(Qx) = f(x)$. Plugging it into Eq. S(2), we have

$$Q_{ip}Q_{jq}Q_{kr}Q_{ls}C_{prqs} = f(x) = C_{ijkl}, \tag{4}$$

which is Eq.(1) in the main text. Once this is satisfied, the material symmetry will be reflected in the stiffness tensor as discussed in the main text and proved in Ref. 9.

Dataset statistics

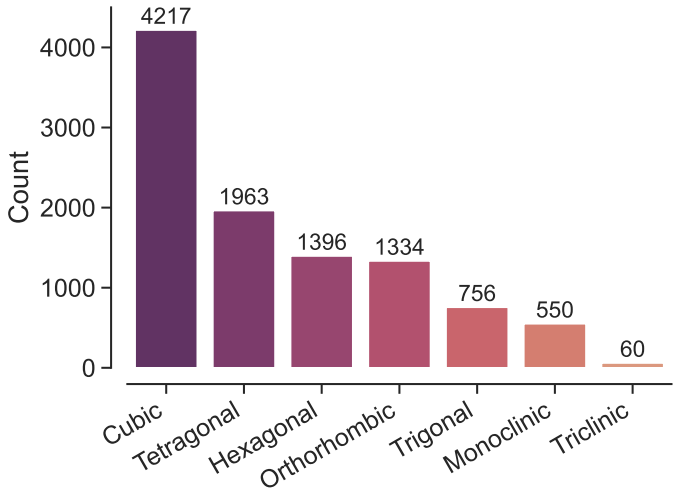

Figure S2: Histogram of the dataset by crystal system. The dataset consists of a total number of 10276 elasticity tensors for inorganic crystals.

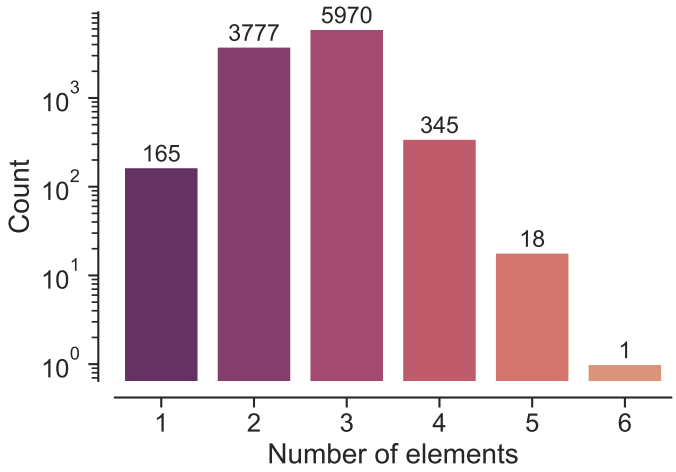

Figure S3: Histogram of the dataset by the number of chemical elements in the crystals.

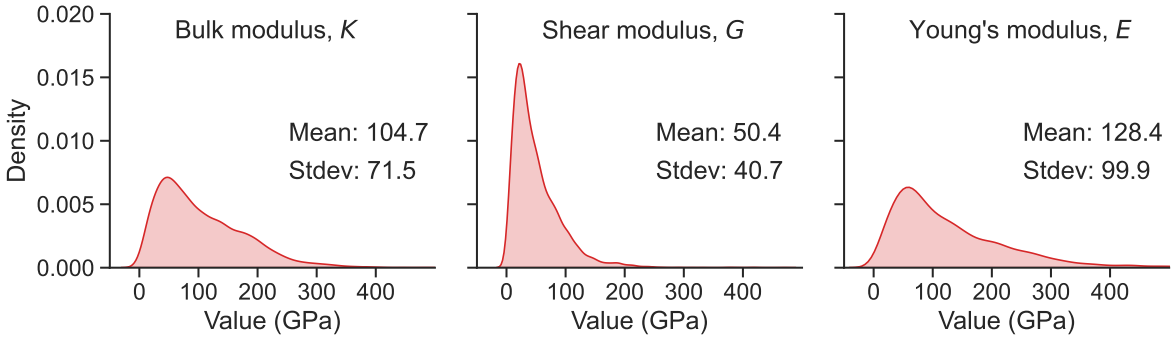

Figure S4: Distribution of the bulk, shear, and Young's moduli in the dataset.

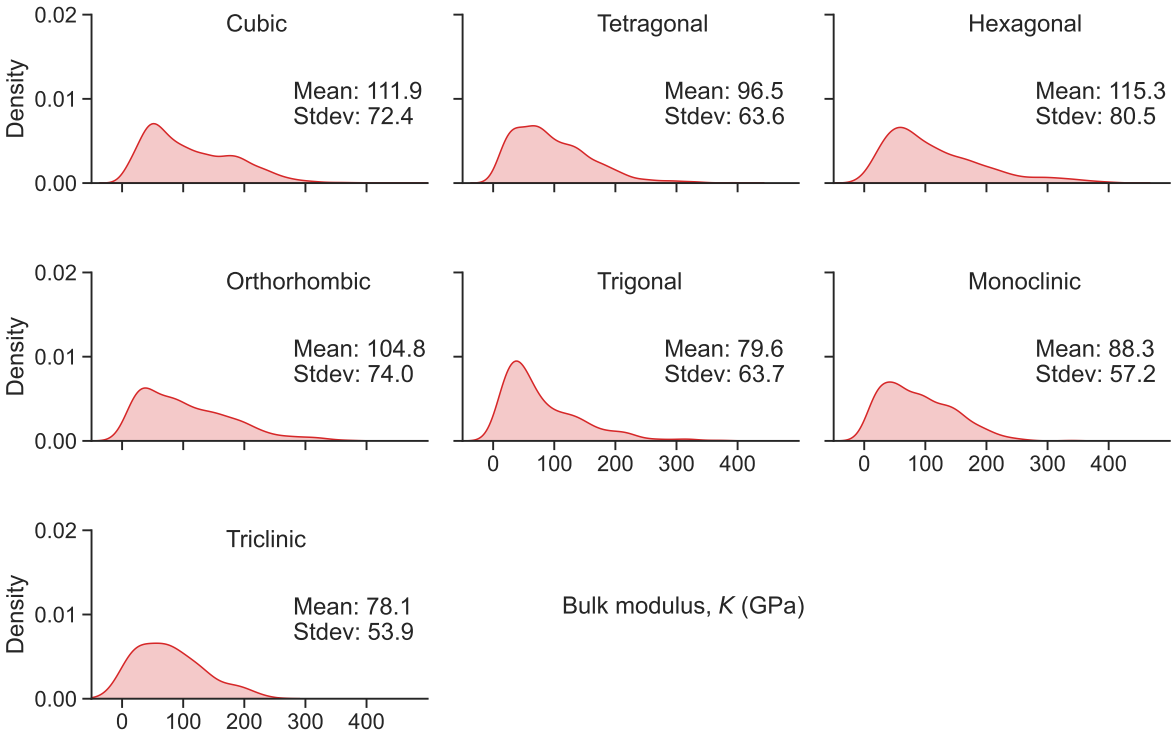

Figure S5: Distribution of bulk modulus in the dataset by crystal system.

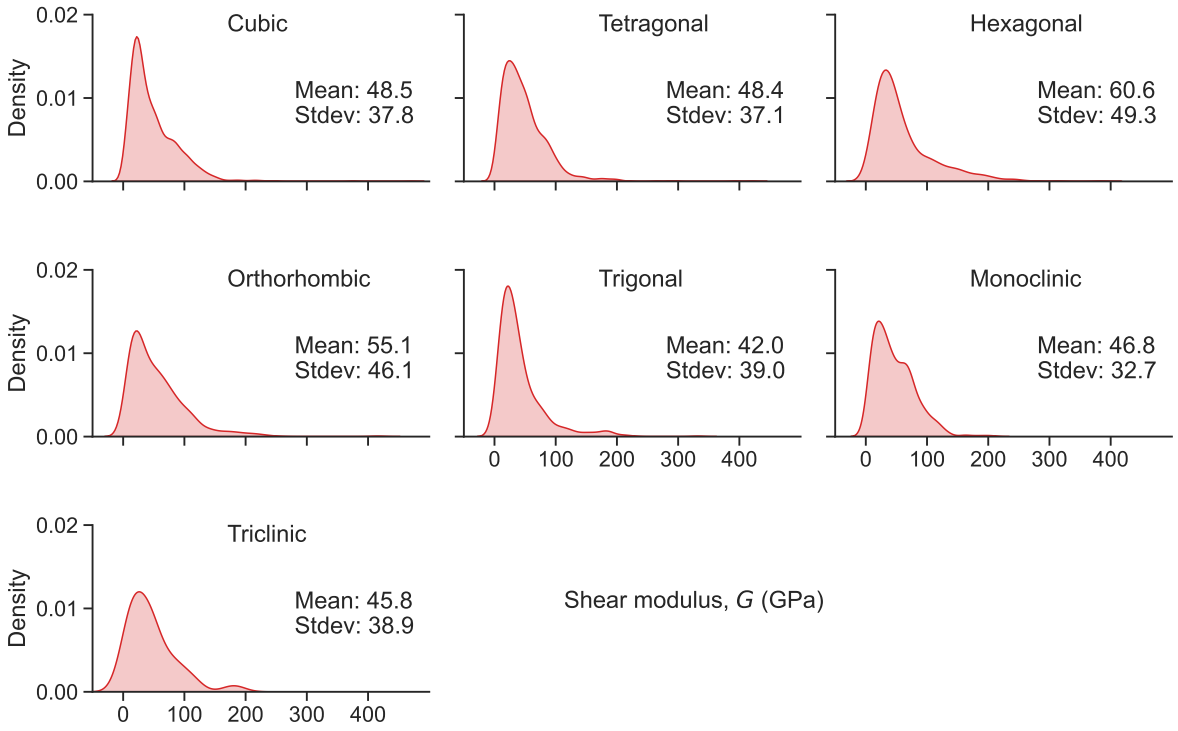

Figure S6: Distribution of shear modulus in the dataset by crystal system.

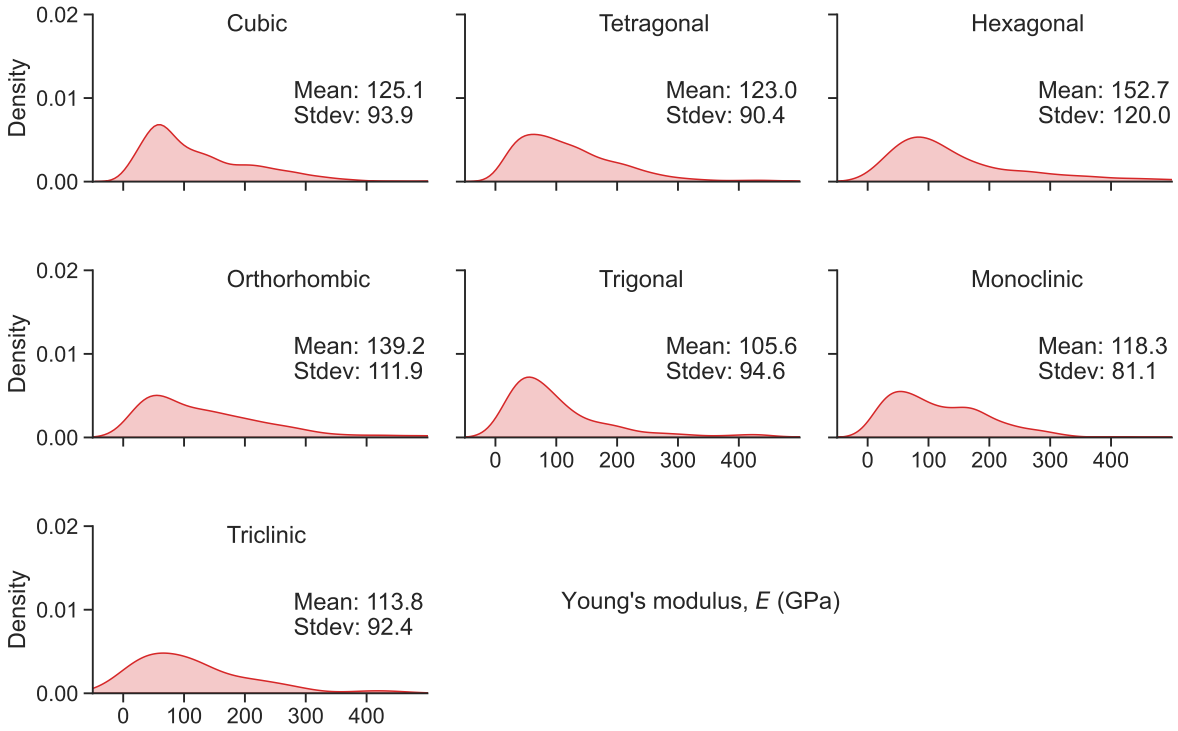

Figure S7: Distribution of Young's modulus in the dataset by crystal system.

Error in strain caused by that in Young's modulus

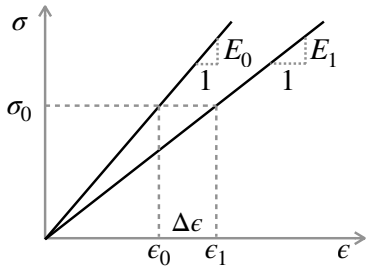

We consider the strain change due to error in Young's modulus under the same stress σ_0. Let $E_0 = 128.4$ GPa (mean of DFT reference values) and $E_1 = E_0 - \Delta E$, where $\Delta E = 20.59$ GPa is the mean absolute error (MAE) of MatTen predictions. We have

$$\begin{aligned} \sigma_0 &= E_0 \epsilon_0 \\ \sigma_0 &= E_1 \epsilon_1 = (E_0 - \Delta E)(\epsilon_0 + \Delta\epsilon). \end{aligned} \tag{5}$$

Solve Eq. S(5), we have

$$\Delta\epsilon = \left[\frac{E_0}{E_0 - \Delta E} - 1\right] \epsilon_0 = 19\%\ \epsilon_0 \tag{6}$$

Test errors

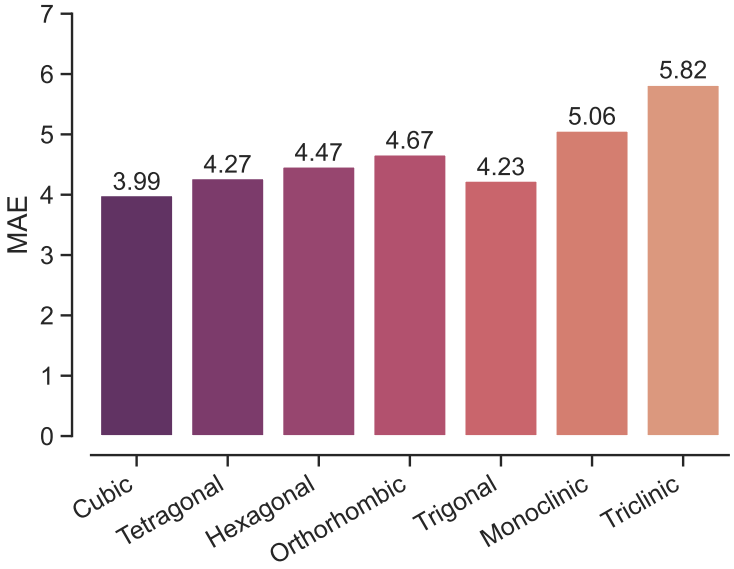

Figure S8: Mean absolute error (MAE) of the elasticity tensor by crystal system. The MAE is computed using the predicted and reference Voigt matrix of the elasticity tensor.

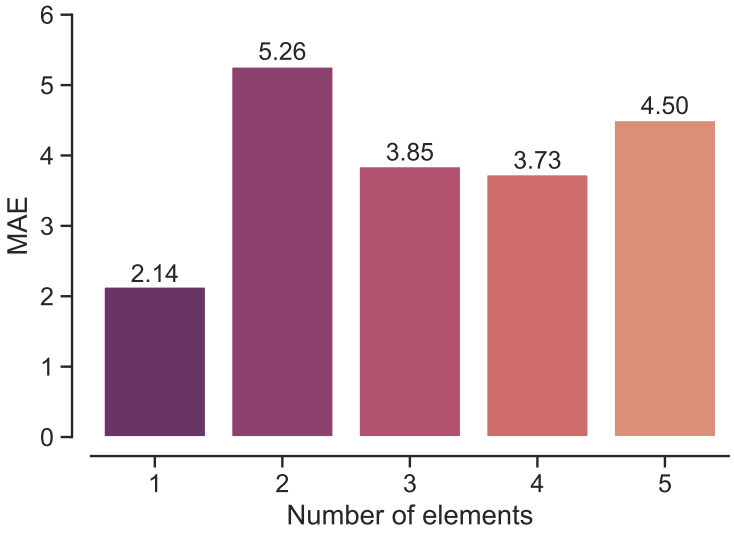

Figure S9: Mean absolute error (MAE) of the elasticity tensor by the number of chemical elements in the crystals. The MAE is computed using the predicted and reference Voigt matrix of the elasticity tensor.

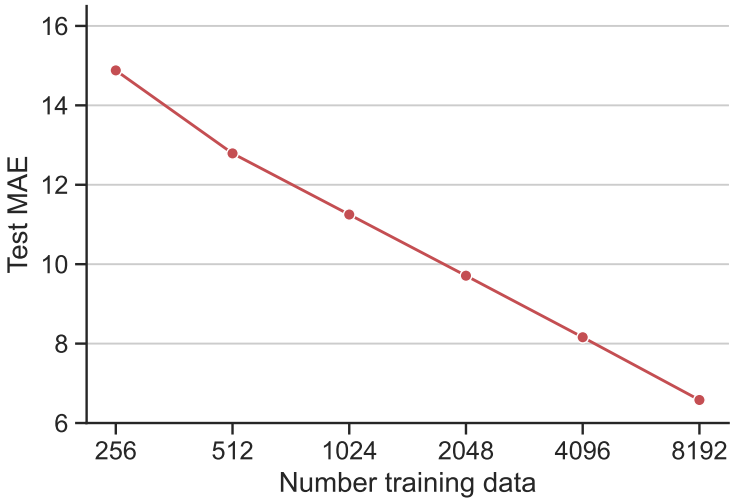

Figure S10: Learning curve of the MatTen model. The MAE is obtained using the predicted and reference elasticity tensors in Voigt notation. The MAE is on the test set, and the number of training data is sampled from the training set.

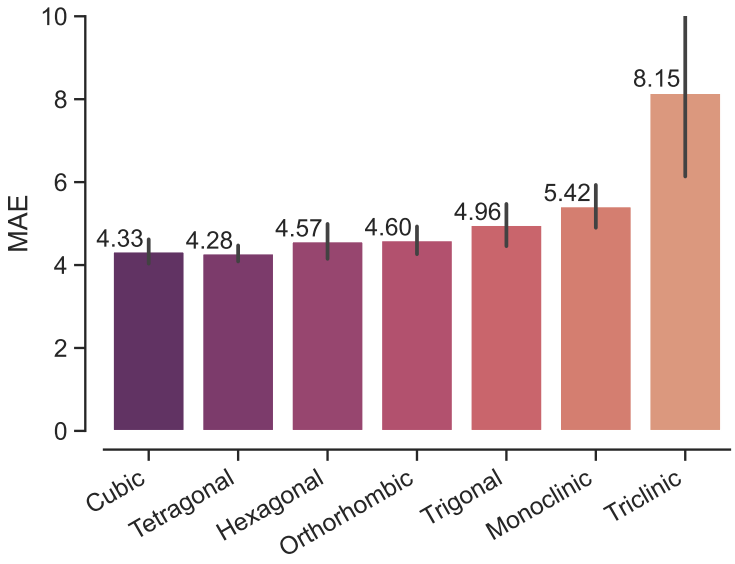

Figure S11: Mean absolute error (MAE) of the elasticity tensor in Voigt matrix computed from ten-fold cross validation. Compare with Fig. S8, where the 9th and 10th fold of the data are used as the validation and test set, respectively.

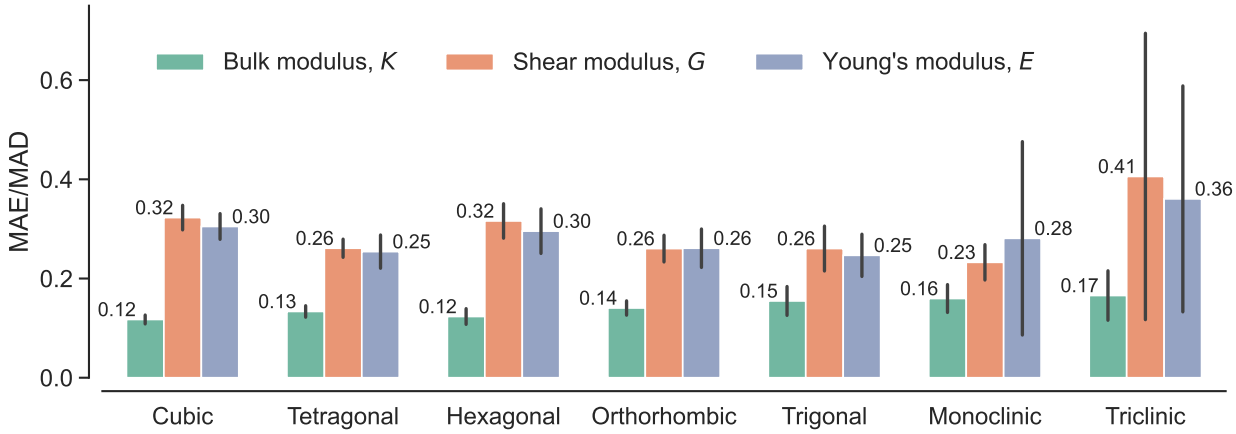

Figure S12: Ten-fold cross validation scaled error (MAE/MAD) on the bulk, shear, and Young's moduli. Compare with Fig. 3d in the main text.

Training on tensor components

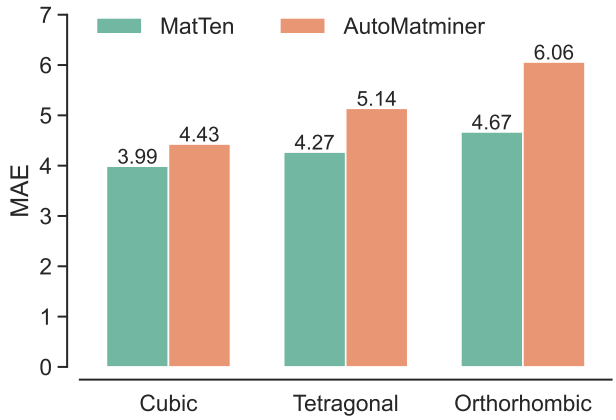

Figure S13: Mean absolute error (MAE) of the elasticity tensor in Voigt matrix. Multiple AutoMatminer models are trained for each crystal system, each model predicting a separate non-zero component of the Voigt matrix in Fig. 1 in the main text. For example, for the orthorhombic crystal system, nine AutoMatminer models are trained.

It is possible to predict the full elasticity tensor by separately modeling its non-zero independent components. Because each crystal system has a different number of non-zero components (Fig. 1 in the main text), this approach requires the treatment of each crystal system separately. To check how this approach works, we consider the cubic, tetragonal, and orthorhombic crystal systems. For each of them, we select the corresponding crystals in the training, validation, and test sets, and then train multiple AutomMatminer models, each with one non-zero component of the full tensor as the target. The mean absolute error (MAE) is shown Fig. S13; also plotted are the MatTen results for comparison.

For the "training tensor components" approach, the performance deteriorates quickly with the tensor complexity, i.e., the number of independent components in the tensor, increasing from cubic to tetragonal, and to orthorhombic. In contrast, the error by MatTen only slightly increases with increased tensor complexity, demonstrating the advantage of the united MatTen approach. MatTen automatically handles all symmetry requirements and thus allows the training using all data, irrespective of the crystal systems. This contributes to the improved performance of MatTen.

Additional results on isotropic properties

Table S1: Prediction of the bulk modulus K, shear modulus G, and Young's modulus E in logarithmic space. K, G, and E are in the units of GPa. The results for MatTen are calculated from a single model, while a separate AutoMatminer model is trained for each property. The value in a pair of parentheses is the standard deviation from an ensemble of five models trained with different initialization. MAE: mean absolute error; MAD: mean absolute deviation.

	$\log_{10}(K)$		$\log_{10}(G)$		$\log_{10}(E)$	
	MAE	MAE/MAD	MAE	MAE/MAD	MAE	MAE/MAD
MatTen	0.046 (0.002)	0.166 (0.006)	0.094 (0.002)	0.331 (0.010)	0.087 (0.002)	0.309 (0.018)
AutoMatminer	0.050 (0.002)	0.187 (0.009)	0.090 (0.002)	0.307 (0.006)	0.086 (0.002)	0.301 (0.009)

Failure analysis

We checked the positive definiteness of the predicted elasticity tensors for the crystal in the test set. The 25 cases with at least one negative eigenvalues are listed in Table S2. For the cubic, tetragonal, and orthorhombic crystals, the failure happens all because of the incorrect prediction of the relative magnitude of the diagonal component and off-diagonal components. For example, for the orthorhombic $Na_4C_4S_4N_4$ crystal (mp-6633), the DFT elasticity tensor is:

$$\begin{bmatrix} 46.7 & 18.1 & 12.2 & 0.0 & 0.0 & 0.0 \\ 18.1 & 30.8 & 10.3 & 0.0 & 0.0 & 0.0 \\ 12.2 & 10.3 & 22.0 & 0.0 & 0.0 & 0.0 \\ 0.0 & 0.0 & 0.0 & 7.4 & 0.0 & 0.0 \\ 0.0 & 0.0 & 0.0 & 0.0 & 8.5 & 0.0 \\ 0.0 & 0.0 & 0.0 & 0.0 & 0.0 & 10.2 \end{bmatrix},$$

while the model predicted is:

$$\begin{bmatrix} 11.4 & 19.7 & 9.9 & 0.0 & 0.0 & 0.0 \\ 19.7 & 24.2 & 3.2 & 0.0 & 0.0 & 0.0 \\ 9.9 & 3.2 & 18.5 & 0.0 & 0.0 & 0.0 \\ 0.0 & 0.0 & 0.0 & 11.8 & 0.0 & 0.0 \\ 0.0 & 0.0 & 0.0 & 0.0 & 10.3 & 0.0 \\ 0.0 & 0.0 & 0.0 & 0.0 & 0.0 & 11.0 \end{bmatrix}.$$

The predicted c_{11} is substantially smaller than the DFT value. For the more complex (in terms of the number of independent components) trigonal crystals, we did not observe any pattern. Nor for the two monoclinic crystals.

Table S2: Number of crystals with negative eigenvalues by crystal system.

Cubic	Tetragonal	Hexagonal	Orthorhombic	Trigonal	Monoclinic	Triclinic
7	7	0	4	5	2	0

Directional Young's modulus

Here we prove that, for cubic crystals,

$$\text{if } S_{1111} - S_{1122} - 2S_{2323} < 0, E_{\mathrm{d}}^{\max} \text{ is along } \langle 100 \rangle \text{ and } E_{\mathrm{d}}^{\max} \text{ is along } \langle 111 \rangle, \tag{7}$$

otherwise,

$$\text{if } S_{1111} - S_{1122} - 2S_{2323} > 0, E_{\mathrm{d}}^{\max} \text{ is along } \langle 111 \rangle \text{ and } E_{\mathrm{d}}^{\max} \text{ is along } \langle 100 \rangle. \tag{8}$$

and

$$\text{if } S_{1111} - S_{1122} - 2S_{2323} = 0, \text{ the materials is isotropic regarding Young's modulus.} \tag{9}$$

The inverse of the directional Young's modulus is

$$E_{\mathrm{d}}(\boldsymbol{n})^{-1} = n_i n_j n_k n_l S_{ijlk}, \tag{10}$$

where S_{ijkl} is the compliance tensor and $\boldsymbol{n}$ is an unit direction vector. For a cubic crystal, the 21 non-zero components can be classified into three groups [2]:

- $S_{1111} = S_{2222} = S_{3333}$
- $S_{1122} = S_{2211} = S_{2233} = S_{3322} = S_{3311} = S_{1133}$
- $S_{2323} = S_{2332} = S_{3223} = S_{3232} = S_{1212} = S_{1221} = S_{2112} = S_{2121} = S_{1313} = S_{1331} = S_{3113} = S_{3131}$.

Substituting these into Eq. S(10), we have,

$$\begin{aligned} E_{\mathrm{d}}(\boldsymbol{n})^{-1} &= S_{1111}(n_1^4 + n_2^4 + n_3^4) + 2S_{1122}(n_1^2n_2^2 + n_2^2n_3^2 + n_3^2n_1^2) + 4S_{2323}(n_1^2n_2^2 + n_2^2n_3^2 + n_3^2n_1^2) \\ &= S_{1111}[1 - 2(n_1^2n_2^2 + n_2^2n_3^2 + n_3^2n_1^2)] + 2S_{1122}(n_1^2n_2^2 + n_2^2n_3^2 + n_3^2n_1^2) + 4S_{2323}(n_1^2n_2^2 + n_2^2n_3^2 + n_3^2n_1^2) \\ &= S_{1111} - 2(S_{1111} - S_{1122} - 2S_{2323})(n_1^2n_2^2 + n_2^2n_3^2 + n_3^2n_1^2) \\ &= S_{1111} - 2(S_{1111} - S_{1122} - 2S_{2323})f. \end{aligned} \tag{11}$$

In the second equality, we have used $n_1^4 + n_2^4 + n_3^4 = (n_1^2 + n_2^2 + n_3^2)^2 - 2(n_1^2n_2^2 + n_2^2n_3^2 + n_3^2n_1^2) = 1 - 2(n_1^2n_2^2 + n_2^2n_3^2 + n_3^2n_1^2)$, in which $(n_1^2 + n_2^2 + n_3^2)^2 = 1$, because $\boldsymbol{n}$ is a unit vector. In the last equality, we have defined $f := n_1^2n_2^2 + n_2^2n_3^2 + n_3^2n_1^2$.

From Eq. S(11), it seen that Eq. S(9) is valid.

In fact, f has its maximum value of $1/3$ along the $\langle 111\rangle$ directions, and the minimum of f is 0 along the $\langle 100\rangle$ directions (derived below). As a result, Eq. S(7) and Eq. S(8) are valid. (Note that Eq. S(11) gives the inverse of the directional Young's modulus.)

Below, we show that the maximum of f is $1/3$ along the $\langle 111\rangle$ directions, and the minimum of f is 0 along the $\langle 100\rangle$ directions.

Let $n_1^2 = a, n_2^2 = b$ and $n_3^2 = c$, we have $a + b + c = 1$ because $\boldsymbol{n}$ is a unit vector. Thus,

$$f = ab + bc + ca = ab + c(b + a) = ab + (1 - a - b)(b + a) = a + b - ab - a^2 - b^2. \tag{12}$$

Let

$$\begin{aligned} \frac{\partial f}{\partial a} &= 1 - b - 2a = 0 \\ \frac{\partial f}{\partial b} &= 1 - a - 2b = 0, \end{aligned} \tag{13}$$

and solve the equations, we have $a = b = c = 1/3$, i.e. $n_1^2 = n_2^2 = n_3^3 = 1/3$, At these values, $f = 1/3$ and we can verify that it is a maximum. This also suggests $\boldsymbol{n}$ is along the $\langle 111\rangle$ family of directions.

The other extreme values of f are located at the boundaries of a (or b or c). Since n_1 is a component of the unit vector, then $n_1 \in [-1, 1]$, i.e. $a \in [0, 1]$. So, the extreme value is obtained when

- $n_1 = 0$, $n_2 = \pm 1$, $n_3 = 0$
- $n_1 = 0$, $n_2 = 0$, $n_3 = \pm 1$
- $n_1 = \pm 1$, $n_2 = 0$, $n_3 = 0$.

These are the $\langle 100\rangle$ directions, at which the minimum is $f = 0$.

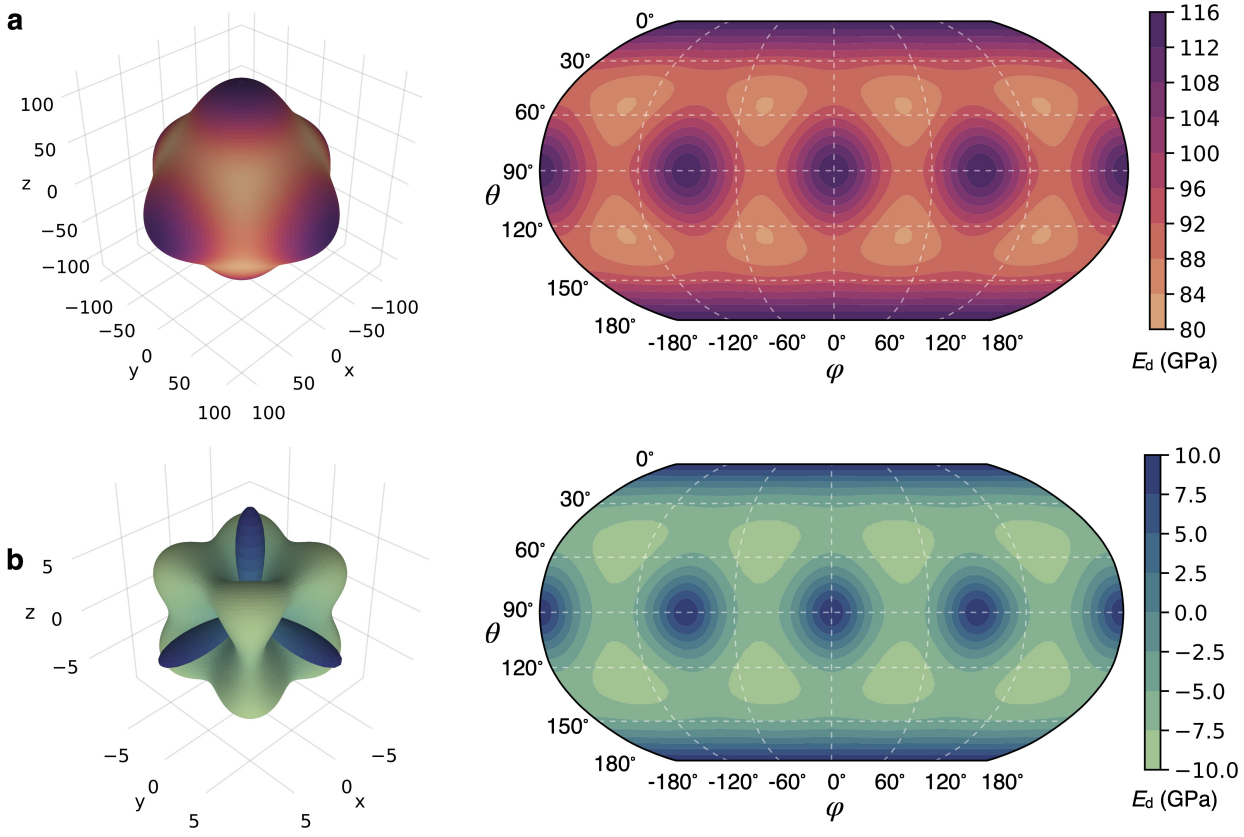

Figure S14: Directional Young's modulus E_d for CaS. (a) DFT reference values. (b) Prediction error between MatTen prediction and DFT reference values.

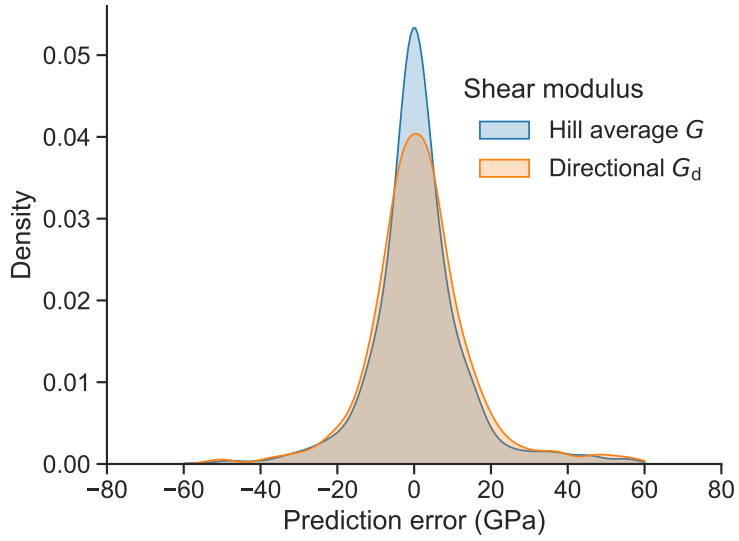

Figure S15: Distribution of the prediction error for shear modulus. The directional shear modulus can be computed as $G_\mathrm{d}(\boldsymbol{n}, \boldsymbol{m}) = (n_i m_j n_k m_l S_{ijkl})^{-1}$, where $\boldsymbol{n}$ and $\boldsymbol{m}$ are two direction unit vectors, and $\boldsymbol{S}$ is the compliance tensor [6]. The data of G_d is obtained by sampling in a way similar to E_d discussed in the main text. The prediction error is the difference between MatTen prediction and DFT reference.

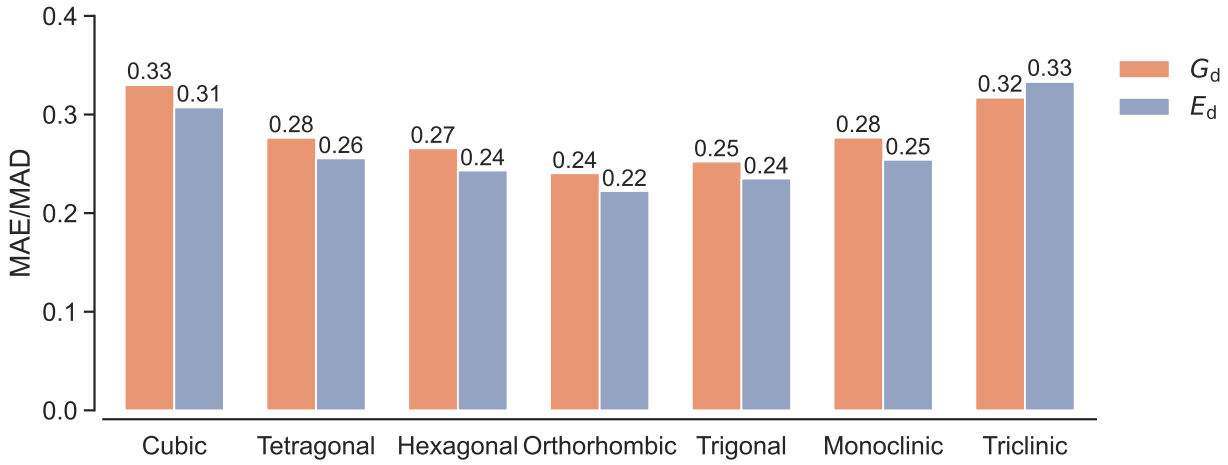

Figure S16: Scaled error in directional shear modulus G_d and Young's modulus E_d. The bulk modulus has no directional dependency, and thus no such plot is presented.

Materials Screening

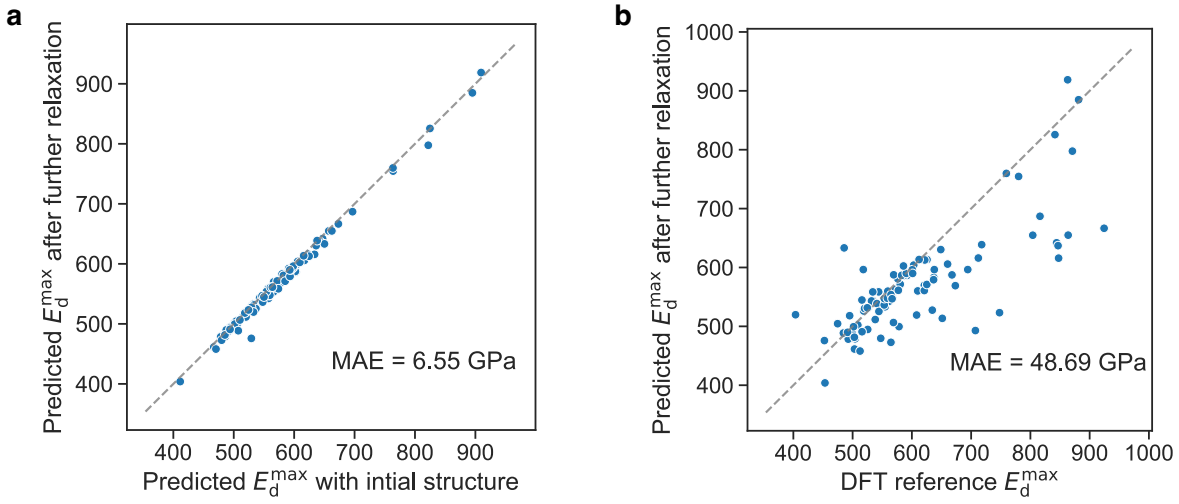

Figure S17: Maximum directional Young's modulus E_d^{max} obtained from DFT and the MatTen model. Each material has two MatTen predictions, one using the crystal structure directly queried from the Materials Project ("Predicted E_d^{max} with initial structure"), and the other using the crystal structure with further geometry optimization ("Predicted E_d^{max} after further relaxation"). The latter has tighter geometry optimization criteria. The DFT reference E_d^{max} is obtained using the latter further optimized geometry.

Fig. S17 shows the E_d^{max} for the 100 new crystals. The MAE between predicted E_d^{max} with initial structure and predicted E_d^{max} with further relaxed structure is 6.55 GPa. It is much smaller than the MAE (22.36 GPa) between MatTen prediction and DFT reference for the test set. This demonstrates the robustness of MatTen with respect to the structure of the input crystal as discussed in the main text. As shown in Fig. S17 b, if we consider the 100 new crystals instead of the test set, the MAE between MatTen prediction and DFT is much higher, with a value of 48.69 GPa. This is expected, since, for the 100 new crystals, we are probing extreme

values at the edge of the training data distribution, while the test set follows the same distribution of the training data. This signifies the importance of further confirmation with more accurate computation (DFT in this case) and even experiments once the search space has been narrowed down via the screening using the model.

Table S3: Polymorphs of elemental cubic metal with $E_{\mathrm{d}}^{\max}$ along $\langle 100 \rangle$ directions and $E_{\mathrm{d}}^{\min}$ along $\langle 111 \rangle$ directions. $\Delta S = S_{1111} - S_{1122} - 2S_{2323}$. Among the crystal structures with the same composition, the one having the lowest energy is called the ground-state polymorph and is stable with respect to phase transition into other structures [14]. The crystal structures and the elasticity tensors of these metals are provided as well. See Data Availability in the main text.

Materials Project ID	Formula	ΔS_{DFT}	$\Delta S_{\mathrm{MatTen}}$	Experimentally observed	Ground-state polymorph
mp-129	Mo	-0.00150	-0.00191	Yes	Yes
mp-146	V	-0.00994	-0.01006	Yes	Yes
mp-17	Cr	-0.00267	-0.00253	Yes	No
mp-90	Cr	-0.00369	0.00055	Yes	Yes
mp-91	W	-0.00056	-0.00042	Yes	Yes
mp-11334	W	-0.00285	-0.00331	No	No
mp-35	Mn	-0.00222	-0.00277	Yes	Yes
mp-1186040	Na	-0.15435	-0.32852	No	No
mp-1184808	K	-0.34397	-0.12334	No	No
mp-949029	Cs	-0.53668	-4.79427	No	No
mp-1239193	Rh	-0.03371	-0.06590	No	No
mp-1187790	Tl	-0.09708	-0.05340	No	No

Model hyperparameters

Table S4: Hyperparameter values obtained by grid search. "fixed" indicates no search, and the value is obtained based on previous work [13, 15]. Full set of the optimal hyperparameters is available in the "pre-trained /20230627" directory of the GitHub repo at: `https://github.com/wengroup/matten`.

Value	Hyperparameter	Searched values
5Å	cutoff radius to construct crystal graph, r_{cut}	4, 5, 6
16	size of one-hot embedding vector for atomic species, c	fixed
8	number of radial basis functions, n	fixed
3	number of interaction blocks	2, 3, 4, 5
32x0o+32x0e+16x1o+16x1e +4x2o+4x2e+2x3o+2x3e+2x4e	irreducible representation of atom features in interaction blocks	fixed
0e+1o+2e+3o+4e	irreducible representation of unit bond vector	fixed
2	number of MLP layers for embedding bond length as in R_c	2, 3, 4
32	number of nodes in the MLP for embedding bond length as in R_c	32, 64

References

[1] Duane C. Wallace. *Thermodynamics of Crystals*. Wiley & Sons, 1972. doi: 10.1119/1.1987046.

[2] John Frederick Nye. *Physical properties of crystals: their representation by tensors and matrices*. Oxford University Press, 1985. doi: 10.1063/1.3060200.

[3] Ellad B Tadmor, Ronald E Miller, and Ryan S Elliott. *Continuum mechanics and thermodynamics: from fundamental concepts to governing equations*. Cambridge University Press, 2012. doi: 10.1017/CBO9781139017657.

[4] Sobhit Singh, Logan Lang, Viviana Dovale-Farelo, Uthpala Herath, Pedram Tavadze, François-Xavier Coudert, and Aldo H Romero. Mechelastic: A python library for analysis of mechanical and elastic properties of bulk and 2d materials. *Computer Physics Communications*, 267:108068, 2021. doi: 10.1016/j.cpc.2021.108068.

[5] Yunguo Li, Lidunka Vočadlo, and John P Brodholt. Elast: A toolkit for thermoelastic calculations. *Computer Physics Communications*, 273:108280, 2022. doi: 10.1016/j.cpc.2021.108280.

[6] Zheng Ran, Chunming Zou, Zunjie Wei, and Hongwei Wang. Velas: An open-source toolbox for visualization and analysis of elastic anisotropy. *Computer Physics Communications*, 283:108540, 2023. doi: 10.1016/j.cpc.2022.108540.

[7] Fedor I Fedorov. *Theory of elastic waves in crystals*. Springer, 1968. doi: 10.1007/978-1-4757-1275-9.

[8] S. Sutcliffe. Spectral decomposition of the elasticity tensor. *Journal of Applied Mechanics*, 59(4):762–773, 1992. doi: 10.1115/1.2894040.

[9] Sandra Forte and Maurizio Vianello. Symmetry classes for elasticity tensors. *Journal of Elasticity*, 43: 81–108, 1996. doi: 10.1007/BF00042505.

[10] George Backus. A geometrical picture of anisotropic elastic tensors. *Reviews of geophysics*, 8(3):633–671, 1970. doi: 10.1029/RG008i003p00633.

[11] Yakov Itin. Irreducible matrix resolution for symmetry classes of elasticity tensors. *Mathematics and Mechanics of Solids*, 25(10):1873–1895, 2020. doi: 10.1177/1081286520913596.

[12] Mario Geiger and Tess Smidt. e3nn: Euclidean neural networks. *arXiv preprint arXiv:2207.09453*, 2022.

[13] Nathaniel Thomas, Tess Smidt, Steven Kearnes, Lusann Yang, Li Li, Kai Kohlhoff, and Patrick Riley. Tensor field networks: Rotation-and translation-equivariant neural networks for 3d point clouds. *arXiv preprint arXiv:1802.08219*, 2018.

[14] Christopher J Bartel. Review of computational approaches to predict the thermodynamic stability of inorganic solids. *Journal of Materials Science*, 57(23):10475–10498, 2022. doi: 10.1007/s10853-022-06915-4.

[15] Simon Batzner, Albert Musaelian, Lixin Sun, Mario Geiger, Jonathan P Mailoa, Mordechai Kornbluth, Nicola Molinari, Tess E Smidt, and Boris Kozinsky. E (3)-equivariant graph neural networks for data-efficient and accurate interatomic potentials. *Nature communications*, 13(1):2453, 2022. doi: 10.1038/s41467-022-29939-5.